
Article:
Kassotakis, N, Sarhosis, V orcid.org/0000-0002-8604-8659, Peppa, MV et al. (1 more author) (2021) Quantifying the effect of geometric uncertainty on the structural behaviour of arches developed from direct measurement and Structure-from-Motion (SfM) photogrammetry. Engineering Structures, 230. 111710. ISSN 0141-0296

https://doi.org/10.1016/j.engstruct.2020.111710

Quantifying the effect of geometric uncertainty on the structural behaviour of arches developed from direct measurement and Structure-from-Motion (SfM) photogrammetry

N. Kassotakis[1], V. Sarhosis[1,2], M. V. Peppa[1], J. Mills[1]

[1]School of Engineering, Newcastle University, Newcastle upon Tyne, NE1 7RU, UK

[2]School of Civil Engineering, University of Leeds, Leeds, LS2 9JT, UK

Abstract

The aim of this paper is to quantify the effect of geometric uncertainty on the structural behaviour of arches developed using traditional geospatial and remote sensing techniques. Geometric models of twenty-five dry-jointed, rigid block arch specimens were developed using the proposed "*Image2DEM*" framework, encompassing the Structure-from-Motion (SfM) photogrammetry pipeline. Assessment of the framework was carried out with respective geometric models developed from tape measurements, in terms of geometry and structural behaviour. The geometric variables investigated were the: a) joint inclination angle; b) joint mid-point location; c) joint length; d) block volume; and e) block centroid location. Concerning structural behaviour, experimental testing of the arch specimens was numerically simulated with the Discrete Element Method (DEM), and the stiffness, load multiplier and normal forces between joints were obtained. Results showed that even small variations (approx. 8%) between geometric models developed from SfM photogrammetry and tape measurements can influence the collapse load and stiffness of the arch by more than 10% and 46% respectively. Also, of the geometric variables investigated, the joint inclination angle was found to influence the collapse load the most. These findings highlight the importance of developing accurate geometric models, and subsequent employment of accurate geometric data acquisition techniques, to reliably capture the structural behaviour of arches. Although an investigation on arch specimens constructed in the laboratory is demonstrated here, the developed outcomes have important implications for the broader topic of data-driven masonry diagnostics using SfM photogrammetry and high-level numerical modelling using micro-modelling strategies such as the DEM.

Keywords: SfM photogrammetry, masonry, discrete element method, geometric model, geometric irregularity, geometric uncertainty

***Corresponding author:** Dr Vasilis Sarhosis, School of Civil Engineering, University of Leeds, Leeds, LS2 9JT, UK

1. Introduction

Masonry is a composite material consisting of masonry units bonded together with or without mortar. Although masonry is very easy to construct, its mechanical behaviour is non-linear and thus complex to predict. Masonry is weak in tension and strong in compression. In fact, mortar joints act as planes of weakness in masonry. The need to predict the in-service and load-carrying capacity of masonry has led to the development of computational strategies which are characterised by different letters of complexity [1]. These range from considering masonry as an anisotropic continuum (macro-modelling strategy) to the more detailed ones considering masonry as an assemblage of units and mortar joints (micro-modelling strategy). Given the importance of the masonry unit-to-mortar interface on the structural behaviour of aged and historic masonry structures, micro-modelling approaches are better adopted to simulate their in-service and load-carrying capacity [1, 16].

However, past research has clearly demonstrated that a vital aspect when modelling masonry structures based on the micro-modelling approach is the accuracy in which the geometry of the masonry structure is transferred to the numerical model. According to Heyman [2], geometric changes in masonry structures can greatly influence their mechanical response. Similar findings have also been confirmed by other researchers. For example, through parametric studies, [3-7] many researchers found that the stability of arches will be affected when variations in the inclination angle of arch joints and the joint length between voussoirs. Another group of researchers have also carried out probabilistic studies on the effects of geometric uncertainty with the Monte Carlo simulations, such as the seminal study [8]. This specific approach, subsequently extended to arch vaults [9], arches with support displacement [10], buttressed arches [11], and dynamically loaded arches [12] suggested that especially for the case of masonry arches, the effect of geometric uncertainty on the structural capacity can be particularly pronounced. Furthermore, Szakály *et al.* [13] and Napolitano *et al.* [14] showed that the bonding pattern in masonry wall panels significantly influences the failure mode and load-carrying capacity of masonry. Also, apart from the bonding pattern, researches [15], [16] have demonstrated that the size of the blocks will also affect the structural capacity of the masonry structure. Although the aforementioned studies demonstrate that the micro-geometry (i.e. the size of the blocks, location and length of mortar joints) in a masonry structure would affect the global structural capacity of the structure, past studies on numerical modelling of masonry [17-20] neglect to use detailed geometrical models but rather use simplified, idealized or ad-hoc geometric models which are easier and faster to obtain.

Over the last two decades, advances in geomatics techniques such as laser scanning and Structure-from-Motion (SfM) photogrammetry have started to drastically change the building industry since such techniques can rapidly and remotely harvest digital geometric records of objects and features in a point cloud format [21-23]. SfM photogrammetry is a passive remote sensing method in which, interest points (IPs) are detected in overlapping images of a structure and used to reconstruct a point cloud using common feature matching and triangulation [24]. Compared to SfM photogrammetry, terrestrial laser scanning (TLS) is an active remote sensing method. Time-of-flight scanners, which are more relevant to applications of masonry structures, measure distance by timing the emission of a pulse of laser energy to the detection of the reflected signal [25]. Both SfM photogrammetry and TLS have been employed with success to accurately and rapidly obtain structural surveying of complex in geometry masonry structures [26-29].

Given the diffused nature of the Finite Element Method (FEM), a huge scientific intent has been dedicated to developing geometric models within the macro-modelling strategy from the geometric data of both TLS and SfM photogrammetry. One such approach is through directly converting a point

cloud into FEM geometric models pioneered by Hinks [30] and since extended [31-33] for three-dimensional geometric models of rubble masonry. Another approach entails the conversion of a triangulated mesh directly into a FEM geometric model. For instance, Conde *et al.* [34] recently developed a 3D geometric model of a full-scale, multi-span masonry arch bridge, by converting a triangulated mesh into a FEM geometric model. D'Altri *et al.* [35] also converted the mesh of a historic leaning tower into both FEM and finite element limit analysis (FELA) geometric models. Another approach entails the employment of non-uniform rational basis spline (NURBS) for geometric model development. Indicatively, Sánchez-Aparicio *et al.* [36], employed the NURBS to develop FEM geometric models of a historic masonry church from the data of SfM photogrammetry. The same research group [37] also carried out another structural analysis of a historic masonry structure with geometric model development carried out with a similar approach. Also, Korumaz *et al.* [38] carried out a structural analysis of a leaning minaret with the FEM with a NURBS-based approach based on TLS data. Finally, another, less common approach entails developing a geometric model through the employment of a building information model (BIM). Rolin *et al.* [39] employed this approach for the structural analysis of a historical church.

At the same, various investigators have developed geometric models within the micro-modelling strategy, directly from orthoimages (i.e. orthoimagery). Acary *et al.* [40] paved the way for this approach by using an orthorectified image (from conventional photogrammetry) for the structural analysis of a historic masonry structure. The employed non-smooth-contact-dynamics (NCSD) numerical method showed a realistic failure mode owing to the actual geometry of a full-scale building façade. Later on, both LA and FEM geometric models of various multi-span arch bridges were developed by manually extracting the contours of the arches from the orthoimagery of TLS in [41]. Based on the effectivity of the latter approach, many more recent investigations followed on cultural heritage masonry structures [21-23,42] and masonry arch bridges [43-45] employing both SfM photogrammetry and TLS. For such studies, it was well-understood that geometric models developed from geomatics techniques are more appropriate in capturing the actual structural behaviour than respective idealized or ad-hoc, yet a degree of geometric uncertainty remains, according to the employed technique. However, only a few studies have investigated the effect of this type of geometric uncertainty. For instance, Morer *et al.* [44] developed geometric models of masonry arches from a total station and SfM photogrammetry. An error of the arch span equal to 2.32% was associated with an error in collapse load and the critical load position of 4% and 6% respectively. Furthermore, Riveiro *et al.* [46] found the collapse load and critical load position varied by up to 19% between geometric models of arches developed by SfM photogrammetry and ground-penetrating radar. De Arteaga and Morer [47] simulated both idealized and accurate masonry arches developed from a total station. For all the idealized masonry arches simulated, 81% of the obtained collapse loads were higher than the accurate. These studies demonstrate that even when employing geometric models developed from geomatics techniques, geometric uncertainty exists and can significantly affect the structural behaviour, especially the collapse load and critical load position (i.e. the ultimate limit states). However, a lack of comprehensive understanding remains on the effect of geometric uncertainty for both the serviceability (i.e. in-service loads, stiffness and internal forces) and ultimate limit states of masonry structures. Moreover, the critical types and quantities of geometric uncertainty, significantly affecting the structural behaviour of masonry structures, remain unknown.

The aim of this paper is to quantify the effect of geometric uncertainty on the structural behaviour of 25 arch specimens developed from SfM photogrammetry and direct measurements (with a tape). Geometric models of the arch specimens tested in the laboratory were developed using the structural analysis software 3DEC based on the Discrete Element Method (DEM). Within DEM, arch specimens

were represented by rigid blocks, separated by dry joints (i.e. zero thickness interfaces). The variables of geometric uncertainty investigated were: a) joint inclination angle; b) joint midpoint location; c) joint length; d) block volume; and e) block centroid location. It should be noted that the determination of the exact reason behind the variation in geometry exceeds the scope of this paper; which is to merely document the existing geometric uncertainty and the resulting structural behaviour uncertainty. Structural behaviour of the arch specimens investigated concerned the: a) stiffness; b) load multipliers; and c) normal forces between joints at hinges during load application. The paper is organized as follows: Section 2 describes the experimental testing, employed as a case study; Sections 3, 4, 5 and 6 detail the three-stage, "*Image2DEM*" framework employed on the case study; Sections 7 reports the results and discussion of the geometric and structural behaviour uncertainty, for the case study, and Section 8 contains the conclusions.

2. Case study: experimental testing of 25 arch specimens

The experimental test of 25 arch specimens carried out by Stockdale *et al.* [48] has been used for the validation of the computational model and case study for application proposed framework (as shown in Figure 3a-b). The arch specimen had a span of 66.30 cm and a rise of 31.71 cm. The arch thickness was 5.63 cm and the width was 9.96 cm. Effectively, the experiment consisted of 25 quasi-static horizontal loading tests of 25 geometrical variations (herein termed arch specimens) to investigate the limiting mechanism to activate collapse of arches subjected to hinge control. These geometrical variations were developed by maintaining the same macro-geometry (span, rise, thickness, as shown in Figure 3e) and altering the micro-geometry (joint location, as shown in Figure 3f). The construction method of the arch is shown in Figure 1. It's noteworthy that the structural surveying of the arch specimens was carried out by tape measurements of the blocks and final constructed arch, of which the measurements are reported in [48].

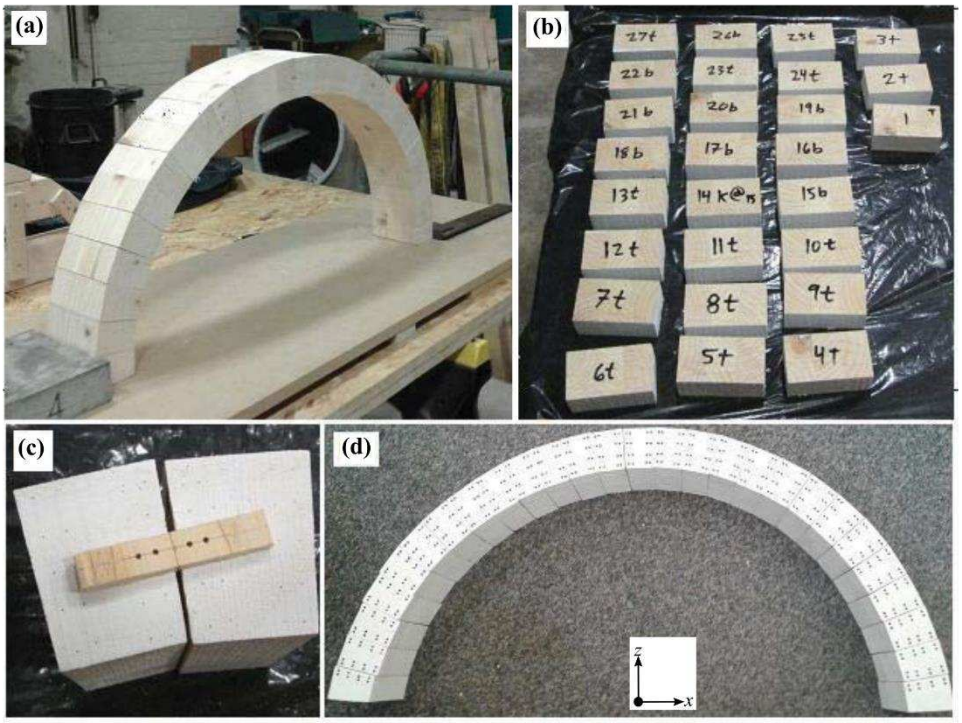

Figure 1. Experimental testing of 25 arch specimens [48]. Construction of arch specimens: (a) initial arch; (b) block measurement and denomination; (c) block alignment; and (d) final arch.

With regard to the structural analysis of masonry arches under both horizontal and vertical loads, various investigations can be found in the literature. The vast majority of investigators have employed limit analysis (LA) formulations. For instance, Misseri *et al.* [49] proposed a novel kinematic LA model for the collapse load of point masonry arches under quasi-static load which was validated experimental and numerical results (i.e. DEM models). Another study proposed a method of safety evaluation of various arches by use of the two limiting equilibrium thrust lines [50]. Nodargi and Bisegna [51] proposed LA analysis models capable of predicting complex failure models through the implementation of joints or varying inclination in both arches and buttresses. carried out the structural analysis of masonry arches with various LA approaches. Galassi *et al.* [52] demonstrated the efficacy of the LA-based software, entitled "*Brickwork*" for the structural analysis of arches and monumental masonry structures of complex geometry. More recently, some studies have also been carried out with the FEM [53] and DEM [16,54]. Whilst these approaches are more computationally demanding, and difficult to implement, they are advantageous in the fact that they provide both the in-service and collapse behaviour, in comparison to only the collapse behaviour within the LA. The reasoning for the employment of the DEM was based on this advantage within this study.

3. The employed "*Image2DEM*" framework

In this section, the three-stage "*Image2DEM*" framework developed in this study is described. This includes: a) Stage 1 - 3D reconstruction; b) Stage 2 - geometric model development; and c) Stage 3 - structural analysis. A flowchart of the proposed framework is shown in Figure 2 and a detailed description of the steps at each stage is shown below. The presented case study is used to depict every step in the flow line.

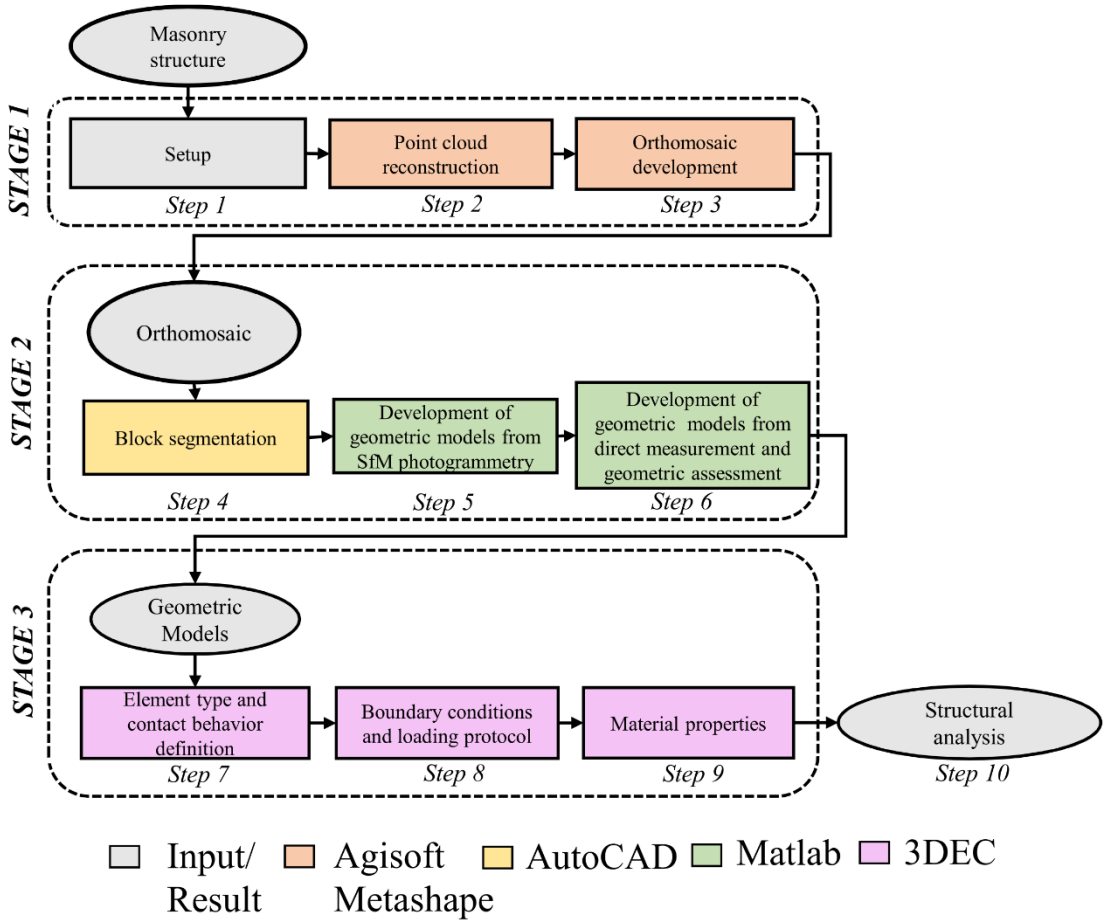

Figure 2 Flowchart of the "Image2DEM" framework.

4. 3D reconstruction with SfM photogrammetry

4.1 Setup

In Step 1, the preparatory planning before employing the SfM photogrammetry pipeline was carried out. This includes the selection of the image capture equipment, image capture network, ground control points(GCPs), and carrying out the image capture. The following paragraphs describe each phase.

4.1.1 Camera sensors employed

Images were captured with the smartphone camera (Sony IMX260 dual-pixel integrated into Samsung Galaxy S7). The reasoning behind the choice of this equipment was to assess the framework with low-cost equipment, often available to structural engineers, in a real-world scenario. The characteristics of the camera sensor are shown in Table 1, where VSS is the vertical sensor size, HSS is the horizontal sensor size and f is the nominal focal length. With the formulas (1) and (2), the horizontal viewing angle of lens (β_h) and vertical viewing angle of lens (β_v) can be calculated [29];

$$\beta_v = 2 \times \tan^{-1}\left(\frac{VSS}{2\times f}\right) \quad (1)$$

$$\beta_h = 2 \times \tan^{-1}\left(\frac{HSS}{2\times f}\right) \quad (2)$$

Table 1. Characteristics of the camera sensor.

Camera characteristic	Unit	Smartphone
Horizontal sensor size (*HSS*)	mm	6.7
Vertical sensor size (*VSS*)	mm	5.5
Nominal focal length f)	mm	4.2
Horizontal pixel number (*HN*)	Pixels	4032
Vertical pixel number (*VN*)	Pixels	3024
Horizontal viewing angle of lens (β_h)	degrees	68.9
Vertical viewing angle of lens (β_v)	degrees	89.0

4.1.2 Ground control points (GCPs)

For the scaling and orientation of SfM photogrammetry point cloud, control information was necessary. This was provided through GCPs. A total of 12 black and white targets of a 6 mm diameter were surveyed with a Leica MS60 total station and employed as GCPs. The total station surveying was carried out by intersection and the achieved RMSE error was equal to 3 mm.

4.1.3 Image network definition and image capture

Apart from the inherent camera properties, there are image network-dependent parameters such as the camera tilt angle (α_t) and working distance (WD). Here the term, maximum ground sampling distance (GSD_{max}) is introduced, calculated from equation (2) [29]. In remote sensing, the GSD_{max} equals the distance between the centre of two consecutive pixels on the target surface and is a spatial resolution used to describe the image quality. The smaller GSD_{max}, the better the quality of the end-product of the SfM-photogrammetry is. At the same time, the field-of-view (FOV) must also be taken into consideration while defining the image network, as calculated from (4) [29]. This effectively defines the quantity of the target surface area captured. The combination of FOV and GSD_{max} will determine the required image network.

$$GSD_{max} = \frac{WD \times HSS \times \cos(\beta_v)}{f \times HN \times \cos(\alpha_t + \beta_v/2)} \quad (3)$$

$$FOV = \frac{WD^2 \times HSS}{2 \times f} \times \left(\frac{\cos(\beta_v/2)}{\cos(\alpha_t - \beta_v/2)} + \frac{\cos(\beta_v/2)}{\cos(\alpha_t + \beta_v/2)}\right) \times \left(\tan(\alpha_t + \beta_v/2) + \tan(\alpha_t - \beta_v/2)\right) \quad (4)$$

In this investigation, a GSD_{max} comparable to the width of the discontinuities of the arch was desirable (less or equal to 1 mm, substantially smaller than 5 mm used in [22]). Due to the requirements of the GSD_{max} , a WD of 0.5 m from the face of the arch was calculated from Table 2 as suitable. Finally, due to the given WD and resulting FOV, image acquisition, image capture consisted of four vertical and two oblique (-45 and 45 degrees) image capture sets at six different heights above floor level.

Table 2. The variation of the field of view (FOV) and ground-sampling-distance (GSD_{max}) for the variation of the working distance (WD).

WD (m)	FOV (m^2)	GSD_{max} (mm)
0.50	0.57	0.09
1.00	2.29	0.19
1.50	5.16	0.28

2.00	9.17	0.38
2.50	14.33	0.47
3.00	20.63	0.57
3.50	28.09	0.66
4.00	36.68	0.76
4.50	46.43	0.85
5.00	57.32	0.95

4.2 Point cloud reconstruction

In step 2, the software Agisoft Metashape Professional ® version 1.5.1 [55] was employed for the reconstruction of the point cloud of the arch specimens with the SfM photogrammetry pipeline. Agisoft Metashape is a low-cost, commercial SfM photogrammetry software which has been used in past research carried out on the 3D reconstruction of masonry structures [27,29,56]. The first phase of the SfM photogrammetry pipeline consisted of the image alignment, resulting in a sparse point cloud and tie points (camera locations). Agisoft Metashape provides multiple settings for image alignment of which the highest alignment setting was chosen. The final pixel error of this alignment was maintained below or equal to one pixel. After the image alignment, the second phase was georeferencing the sparse point cloud by introducing the surveyed GCPs of Section 4.1.2. The GCP coordinates were provided to the software in a text format, directly provided by the total station. The final phase of the SfM photogrammetry pipeline was the reconstruction of the dense point cloud (as shown in Figure 3a). From the options of smoothness and detail within Agisoft Metashape, the high-quality point cloud reconstruction setting was used in conjunction with the aggressive smoothness level.

At this point it should be noted that even though internal precision of the SfM photogrammetry pipeline can be identified via a repeatability control, this was not explicitly carried out since the focus of the study was mostly on developing an end-to-end framework. However, based on past evidence of application other than masonry structures [57], various parameters of the current framework were controlled, that can affect the repeatability of the outcomes. One such parameter that significantly affects the SfM output accuracy is the precision of GCPs (which are translated as marker accuracies in Agisoft). Specifically, tests of a previous study [57] have demonstrated that the variability of different values of GCP's measurement precision can adversely affect the internal precision of SfM processing. To minimise the effect of this parameter in the present study, the GCPs were surveyed with a total station, achieving a mm-level measurement precision. Another important parameter is the tie point accuracy, which has also been found to affect the internal precision of SfM processing [57]. To mitigate the effect of this parameter, tie points of a high error magnitude were removed within an internal process (i.e. the gradual selection tool), following the aforementioned study [57]. A final parameter is the camera model which has also been found to affect the precision of the SfM photogrammetry's outcomes. Specifically, it has been shown that either too few or too many camera parameters within the optimization process can affect the internal precision [57]. Based on this study, an according camera model for the smartphone was chosen with their values estimated in Agisoft Metashape as seen in Table 3; where: f is the focal length; C_x and C_y are the principle point's position on the x and y-axis respectively; B_1 is the affinity; B_2 is the non-orthogonality; K_1, K_2 and K_3 are the radial distortion parameters; and P_1 and P_2 are the decentring distortion parameters.

Table 3. Self-calibration properties of smartphone sensor from Metashape (pixels).

	f	C_x	C_y	B_1	B_2	K_1	K_2	K_3	P_1	P_2
Value	3.1×10^3	-15.51	68.57	-0.15	2.25	-0.07	0.54	-2.08	2.57	2.1×10^{-3}
Error	0.68	0.44	0.54	0.64	0.38	0.00	0.01	0.03	0.03	4.7×10^{-5}

It is also important to note that, concerning the sensitivity of the framework to different noise levels in the SfM photogrammetry model, various types of noise can be referred to. One type of noise comes from the unresolved lens distortion of the SfM bundle adjustment in Metashape, which is particularly relevant in the case of low-cost cameras [58] such as smartphones. The employment of GCPs helped to reduce any unresolved distortions in the present study. It is also noteworthy that the strategic configuration of the GCP (i.e. well-distributed GCPs across the scene and each GCP visible in many images) was also crucial for this, as indicated in multiple previous investigations [59-62]. Another type of noise is related to the imaging configuration which may cause systematic errors. A high image overlap alongside depth variation within the scene is an important consideration to ensure that systematic errors will be removed from SfM outputs. In the present study, the number of optical rays per tie point of Table 4 shows a relatively strong and sufficient imaging configuration. Additionally, another equally important parameter of Table 4 is the ground sampling distance (GSD_{max}) which has also been found to cause noise, when displaying large values [63].In the study, the GSD_{max} was relatively small (i.e. less than the width of the joints, c. 0.1 mm), as calculated from (3).

Table 4. Processing details of Metashape project using the smartphone sensor.

Predefined WD (m)	No of images of the region of interest	Estimated GSD_{max} (mm/pix)	Optical rays per point
0.5	166	0.1	3.2

4.3 Orthomosaic development

In Step 3, an orthomosaic of the arch was developed with Agisoft Metashape, as shown in Figure 3b. Orthomosaics for geometric model development has been successfully used in past research on masonry structures [64,65]. In Agisoft Metashape, a mesh must be developed from the dense point cloud, and then orthomosaic development follows with a user-defined resolution, termed $Res_{orth.}$. In this investigation, the mesh with 30,000 faces developed and the resolution of the orthomosaic was equal to 0.1 mm. Due to the small scale of the experiment and dry joints, an exceptionally small orthomosaic resolution was necessary to enable the definition of the discontinuities of the structure in the orthomosaic. It is anticipated that, for a large-scale structure, blocks have either wider discontinuities or higher colour contrasts between blocks which facilitates discontinuity definition. This means that in a real-life scenario, more reasonable values of $Res_{orth.}$ in the vicinity of 5 mm (as employed in [22]) would be adequate.

5. Geometric model development

5.1 Block segmentation

In Step 4, block segmentation was carried out. This consisted of inserting the orthomosaic into AutoCAD 2019 ® version 23.0 [66], tracing and manually marking the boundaries of each block, as shown in Figure 3c. Though this manual process is recommended for masonry structures of few blocks (e.g. less than one hundred blocks), it could have become tedious to be implemented in a full-scale

masonry structure such as masonry arch bridge. The result of block segmentation was the so-called "*block array"*, consisting of the vertices of each block organized by block and in clockwise order. The blocks of the *block array* were unscaled. The actual size of the blocks was obtained by multiplying the *block array* by the orthomosaic resolution, Res_{orth}. The blocks of the $block\ array_{scaled}$, found in (5) have their actual dimensions.

$$block\ array_{scaled} = (block\ array) \times Res_{orth.} \quad (5)$$

5.2 Development of geometric models from SfM photogrammetry

In Step 5, the geometric model from SfM photogrammetry was developed in a suitable format for the structural analysis, according to the numerical method employed (e.g. LA, FEM, DEM etc.). In this investigation, a geometric model of the arch specimens tested in the laboratory developed in the DEM software 3DEC (see Figure 3d), though the framework could have been employed for other numerical methods of structural analysis. Blocks were developed adopting the *polyhedron* command format of the discrete element method software 3DEC ® version 5.2 [67], using the vertices of the *block array* in a script in Matlab 2019 ® version R2019b [68]. To be able to perform the geometrical assessment of the following paragraph, the geometric models of the SfM photogrammetry and tape measurements needed alignment. A reference point was used, as shown in Figure 3c-d and alignment was by carried out by translating all the coordinates of the $block\ array_{scaled}$ in the x and z-axis direction (the axis common convention is shown in Figure 3c), equal to dx_{align} dz_{align}, from equations (6) and (7) below. It was anticipated that the orientation of the orthomosaic was carried out during the SfM pipeline and thus only translation was necessary to align the geometric models. The blocks of the $block\ array_{aligned}$, found in (8), are aligned.

$$dx_{align} = x_{orth.} - x_{geom.\ model.} \quad (6)$$

$$dz_{align} = z_{orth.} - z_{geom.\ model.} \quad (7)$$

$$\begin{bmatrix} block\ array_{aligned}(:,1) \\ block\ array_{aligned}(:,2) \end{bmatrix} = \begin{bmatrix} block\ array_{scaled}(:,1) - dx_{align} \\ block\ array_{scaled}(:,2) - dz_{align} \end{bmatrix} \quad (8)$$

5.3 Development of geometric models from tape measurement and geometrical assessment

In Step 6, the geometric models from tape measurements were developed, and their geometrical uncertainty was measured. Geometric models were developed with block vertices taken from the experimental testing [48], following the same framework of section 5.2. Two types of geometrical properties were employed to carry out the geometrical assessment. These were: a) the geometrical properties which were arch specimens' span and rise (as shown in Figure 3e.) which were fixed or otherwise invariable parameters due to the method of construction of the arch in the experiment; and b) the variable geometrical properties such as the joint length, joint midpoint location, joint dip (joint inclination angle), the block volume and the block centroid location (as shown in Figure 3f). It is important to note that only the block and joint vertices of the initial arch (i.e. the arch made of free moving blocks of Figure 1a) were measured with both tape measurements and SfM photogrammetry. The properties each of the arch specimens (i.e. block volume, block centroid, joint dip, joint length and joint midpoint) were subsequently calculated as a function of the measured vertices. To estimate the geometric uncertainty, the normalized uncertainty (NU) was used, calculated using the following formula (9):

$$NU = (x^{ref} - x)/\max(x^{ref})\ \% \quad (9)$$

Where x^{ref} and x are geometrical properties of the geometric model from SfM photogrammetry and tape measurements. Additionally, $\max(x^{ref})$ refers to the maximum value of the property group (e.g. a value close to that of the arch rise for the normalized uncertainty of the joint midpoint z-axis properties)

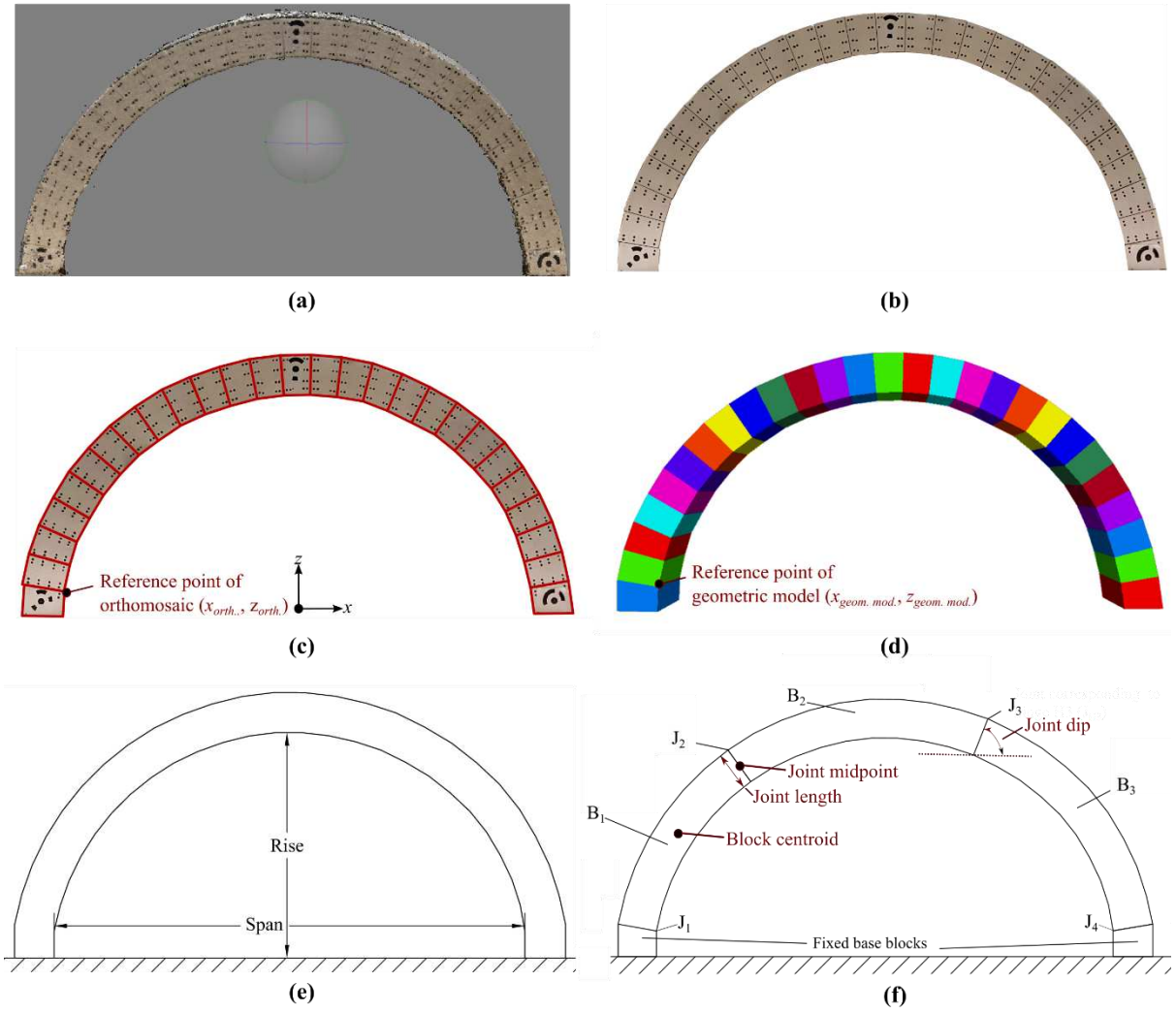

Figure 3. Dry-jointed arch: (a) dense point cloud; (b) orthomosaic; (c) manual block segmentation; and (d) geometric model. Arch specimen number one: (e) invariable geometrical properties; and (f) variable geometrical properties.

6. Structural behaviour with the discrete element method

6.1 Element type and contact behaviour definition

The DEM is an approach that has been widely used to simulate the static and dynamic behaviour of blocky structures. 3DEC is a computational software used to simulate the static and dynamic behaviour of masonry and is based on the DEM. Within the DEM, masonry units (i.e. blocks) are represented as rigid or deformable blocks, which may form any arbitrary geometry. Mortar joints are represented by zero thickness interfaces and governed by appropriate stress-displacement constitutive laws at point contacts between blocks [67]. At all contacts on all blocks, calculations are

made using the force-displacement law and Newton's second law of motion. From known displacements, the force-displacement law is used to find contact forces. Motion of the blocks is calculated using Newton's second law. Block contacts can be face-to-face, vertex-to-face or edge-to-edge type. Finite displacements of the discrete bodies and rotations are allowed which includes the complete detachment of blocks and new contact generation as the calculation proceeds. Forces are considered as linear functions of the actual penetration in the shear and normal directions [69].

The inelastic material properties used within these models were the joint cohesive strength (c), the joint tensile strength (T), and the joint friction angle (φ). According to the adopted joint constitutive model, the structure's behaviour was governed by the joint normal and shear stiffnesses, K_n and K_s in the elastic range. Failure at the joints was either due to tensile or shear failure. The default residual values of the adopted joint constitutive model were a residual cohesive and tensile strength equal to zero. As a residual friction value was not provided, the residual friction was equal to the default. For undamaged joints, the tensile normal force was limited to T_{max} and the shear force was limited to F^s_{max}. The two are found in equations (10) and (11), where T is the joint tensile strength, A_c is the sub-contact area, c is joint cohesive strength and φ is the joint friction angle.

$$T_{max} = -T \times A_c \tag{10}$$

$$F^s_{max} = c \times A_c + F^n \times tan\,\varphi \tag{11}$$

6.2 Boundary conditions and loading protocol

As previously defined, the geometric model is only a geometrical entity. The geometric model, once employed by a numerical method and assigned numerical properties (e.g. material properties, boundary conditions etc.) shall herein be termed, numerical model. The base blocks of the numerical models were fixed, as in the experiment. This was ensured by applying a zero velocity to their centroid (i.e. limiting all degrees of freedom parallel to the x, y and z-axis) within 3DEC. The loading of the arch was according to the experimental applied tilt-table approach [70]. According to this method, a rotation of the tilting plane equal to θ_t, is equivalent to applying a horizontal acceleration of a magnitude λ·g. The load multiplier λ found in the equation (12) below is herein used in all simulations to make results comparable. As will be detailed in Section 6.4.1, the values of the load multipliers were recorded at each hinge formation during the loading phase.

$$\lambda = \tan(\theta_t) \tag{12}$$

6.3 Material properties assigned in the numerical model

Table 5 shows the material properties used for the development of the numerical models. These properties result from calibrating: a) the collapse load (also termed 4th load multiplier in section 6.4.1); and b) the failure mode. Table 6 compares the experimental against the numerical collapse loads for the first 10 arch specimens. In Figure 4a-b, a comparison between the experimental and numerical failure mode of arch specimen No. 6 is shown. A similar failure mode was observed for the rest of the arch specimens (i.e. a four-hinge mechanism).

Table 5. Material properties used in the numerical models.

Mechanical property	Symbol	Unit	Model
Density	ρ	Kg/m^3	500
Joint normal stiffness	K_n	GPa/m	0.15
Joint normal stiffness	K_s	GPa/m	K_n /2.38

Joint cohesive strength	*c*	MPa	0.0
Joint tensile strength	*T*	MPa	0.0
Joint friction	*φ*	°	25.0

Table 6. Comparison of experimental [48] and numerical collapse loads (with the geometric models from tape measurement).

Arch specimen number	Experimental	Numerical	% Error
1	0.32	0.29	9.38
2	0.32	0.29	9.38
3	0.32	0.28	12.50
4	0.32	0.30	6.25
5	0.31	0.31	0.00
6	0.43	0.41	4.65
7	0.42	0.41	2.38
8	0.42	0.39	7.14
9	0.42	0.39	7.14
10	0.40	0.39	2.50

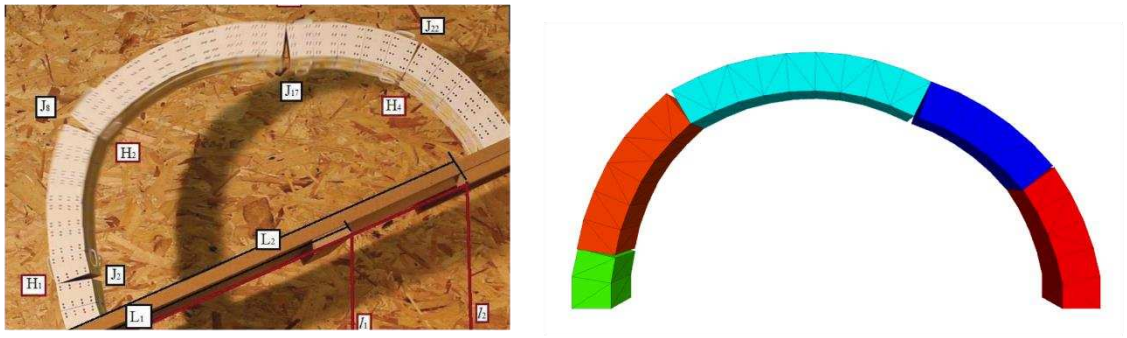

Figure 4. Calibration of: (a) experimental; and (b) numerical failure modes of arch specimen number six.

6.4 Structural analysis

6.4.1 Structural behaviour indices

In Step 10, structural analysis was carried out. Various metrics were employed for assessing the in-service and collapse behaviour of the arch specimens, herein termed structural behaviour indices. To assess the load at which hinge formation occurred, load multipliers were calculated at each hinge formation, symbolized λ^{h1}, λ^{h2}, λ^{h3} and λ^{h4} respectively (see Figure 5a-d). Hinge formation was detected by recording displacement histories of the joints with a *FISH routine* in 3DEC. During the loading of the arch, damage of the 1st, 2nd and 3rd load multipliers (λ^{h1}, λ^{h2}, λ^{h3}) was obtained (i.e. removal of load results in the initial undamaged state). These load multipliers give information about the behaviour of the structure at the in-service behaviour (i.e. serviceability limit states). Moreover, the horizontal stiffness of the arch specimens at the first crack (herein termed stiffness) was calculated by calculating the ratio of the 1st load multiplier (λ^{h1}) toward the horizontal displacement of the block B_2 ($U_{x,B2}$), as shown in formula (13) which also regards the serviceability limit states. Finally, the 4th load multiplier (λ^{h4}) is synonymous with the collapse load and regards the ultimate limit state (i.e. collapse behaviour) of the arch specimens.

$$Stiffness = \frac{(\lambda^{h1})}{U_{x,B2}} \tag{13}$$

To assess the internal forces of the arch specimens at each hinge formation, the joint forces (maximum normal sub-contact forces F_1^n, F_2^n, F_3^n, F_4^n) at each joint were calculated (see Figure 5e.). All the above metrics were calculated with automated processes introduced into 3DEC with a *FISH routine*. It is important to note that within 3DEC, for rigid blocks, all deformability of the system is theoretically lumped at the joints. However, due to the fact of overlapping of contacts, a small amount of interpenetration can be observed. As a consequence of this, the observed structural failure was sequential (i.e. one joint per time, and without activation of the mechanism, until collapse load multiplier λ^{h4} is reached). It is also noteworthy that this sequential failure was governed by the joint stiffnesses K_n,K_s (and the calibration procedure as a consequence).

6.4.2 Structural behaviour uncertainty

To calculate the uncertainty in the structural behaviour of arch specimens, the normalized uncertainty (NU) was employed and calculated using the equation (14):

$$NU = (y^{ref} - y)/\max(y^{ref})\ \% \tag{14}$$

,where y^{ref} and y are structural behaviour indices of the geometric model from SfM photogrammetry and tape measurements accordingly. It is notable that $\max(y^{ref})$ refers to the maximum value of the property type, in order to normalize the uncertainty (e.g. the collapse load multiplier of arch specimen number 25 for the case of load multipliers).

.

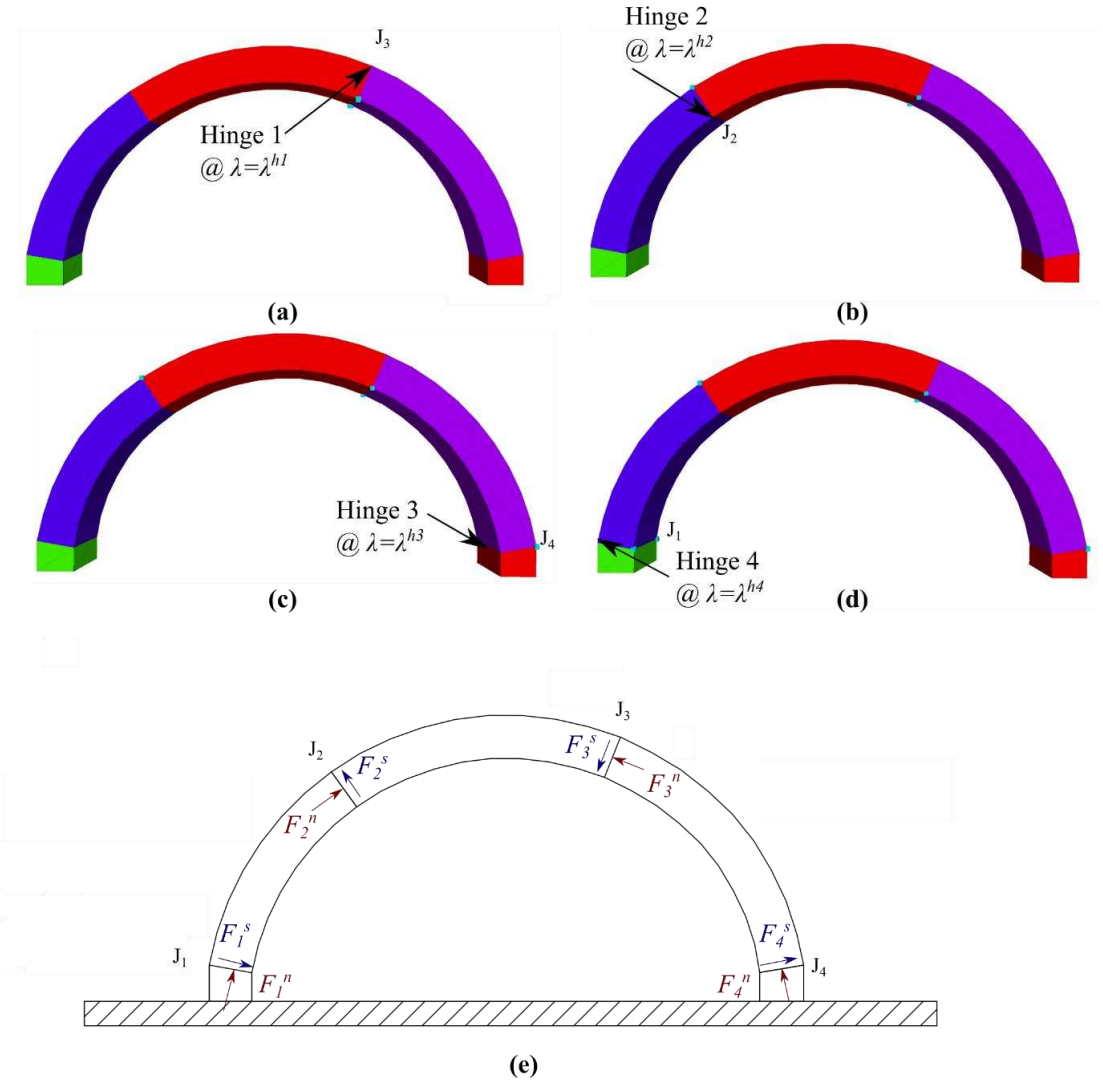

Figure 5. Structural behaviour indices. The load multiplier at each hinge formation: (a) 1st load multiplier (λ^{h1}); (b) 2nd load multiplier (λ^{h2}); (c) 3rd load multiplier (λ^{h3}); and (d) 4th load multiplier (λ^{h4}) (collapse load); (e) forces F_1^n, F_2^n, F_3^n, F_4^n at joints J_1, J_2, J_3 and J_4.

6.4.3 Correlation of geometric and structural behaviour uncertainty

To investigate the correlation between geometric and structural behaviour uncertainty, the well-known Pearson correlation coefficient was calculated using the formula (15), where x and y are any given uncertainty of the geometric model and structural capacity respectively. To avoid the misinterpretation of casual correlations, only values of correlation coefficient (r) larger than 0.8 were treated as valid.

$$r = \frac{(n\times\sum(xy) - (\sum x)\times(\sum y))}{\sqrt{[n\times\sum x^2 - (\sum x)^2] - [n\times\sum y^2 - (\sum y)^2]}} \quad (15)$$

7. Results and discussion

The following subsections present the development and simulation of the 25 geometric models from SfM photogrammetry and tape measurements. First, the geometric uncertainty of the 25 geometric models is reported. Concerning geometric uncertainty, the variables investigated were: a) the joint

midpoint location (x-axis and z-axis), b) joint length and c) joint inclination angle; as well as d) the block volume and e) block centroid location (x-axis and z-axis). Then, the structural behaviour uncertainty was investigated due to geometric uncertainty. The effect of geometric uncertainty was investigated on the: a) load multipliers at each hinge formation; b) stiffness (at the first hinge formation); and c) joint forces at each hinge formation. Finally, a correlation between structural behaviour and geometric uncertainty was investigated.

7.1 Geometric uncertainty

For all the arch specimens, the span and rise normalized uncertainties were equal to 0.6 and 1.5% respectively between the tape measurements and SfM photogrammetry. It is well-understood that span and rise affect the structural behaviour, yet since these variables remain constant, the geometric uncertainty of the blocks and joints is only of concern in this investigation. In Figure 6a-d and Figure 7a-d, the normalized geometric uncertainty of the blocks and joints between the tape measurements and SfM photogrammetry is plotted. From Figure 6a-d and Figure 7a-d, the quantity of the geometric uncertainty was: a) existent and significant for all the joints and block properties; and b) most significant for the joint length and block volume with minima-maxima intervals of -4% to 7% and 4% to 8% accordingly. Furthermore, from Figure 7a-d, the geometric models of the tape measurements were slightly larger, compared to those of SfM photogrammetry. The cause of geometric uncertainty may have been due to: a) gross errors of tape measurement; b) errors of SfM photogrammetry measurement; and c) errors in alignment (scaling and orientation) of the geometric models. Concerning the consistency of joints errors of Figure 6a-d, this is given to that, during the experimental testing, only the block and joint vertices of the initial arch assembly were measured, as aforementioned (and not the 25 arch specimens *per se*). Since each arch specimen was a four-block assembly composed of the blocks and joints of the initial arch, multiple arch specimens shared common joints, leading to consistency in some of the joint errors.

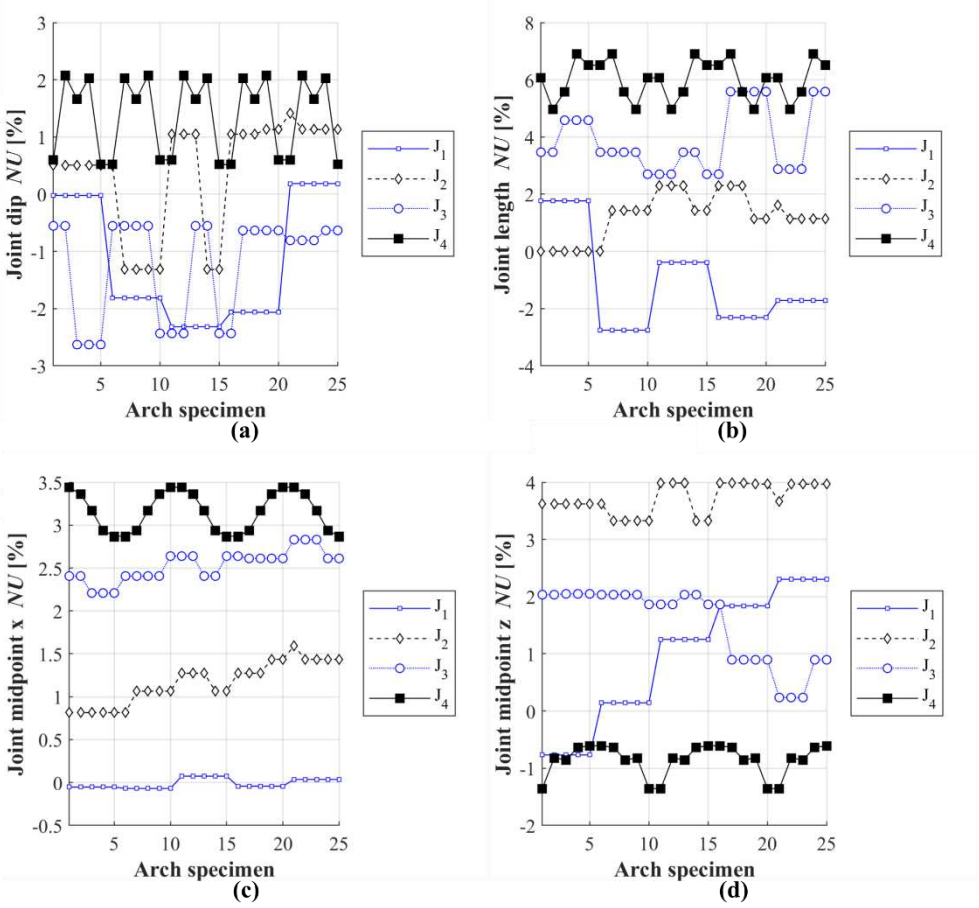

Figure 6. Normalized geometric uncertainty of: (a) joint dip; (b) joint length; (c) joint midpoint x; and (d) joint midpoint z (note the difference in scale).

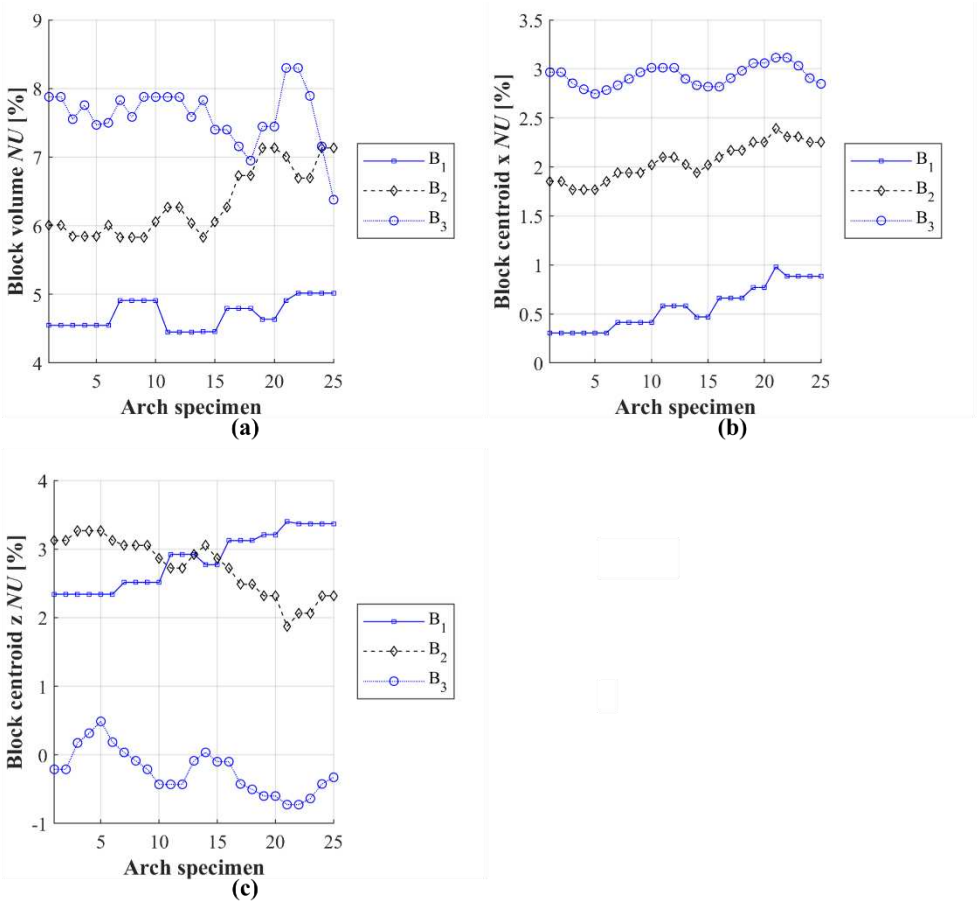

Figure 7. Normalized geometric uncertainty of: (a) block volume; (b) block centroid x; and (c) block centroid z (note the difference in scale).

7.2 Influence of geometrical uncertainty on the load multipliers and stiffness

Figure 8a-e shows the magnitude and distribution of all the load multipliers and the stiffness of the geometric models from SfM photogrammetry and tape measurements. In Figure 8f, the normalized uncertainty of all the load multipliers and stiffness is plotted to illustrate the variance between the curves of Figure 8a-e. Figure 8a-f suggests that the effect of the geometric uncertainty was: a) existent and accumulative for all the load multipliers; b) most significant on the 4th load multiplier (collapse load), i.e. the ultimate limit states, with a minima-maxima interval ranging from -1% to 10%. From Figure 8a-f, the effect of the geometric uncertainty was and even more significant on the stiffness than the load multipliers, with a minima-maxima interval ranging from 2% to 46%. These findings are similar to past research [44,46] in which it was found that geometric uncertainty significantly affects not only the ultimate limit states (i.e. collapse load λ^{h4}) but also has a significant influence on the serviceability limit states (i.e. λ^{h1}, λ^{h2}, $\lambda^{h3}$and stiffness). It is important to note that the values of Figure 8f which refer to the normalized uncertainty may have negative values, however, as is evident from Figure 8a-d, the load multipliers are always positive.

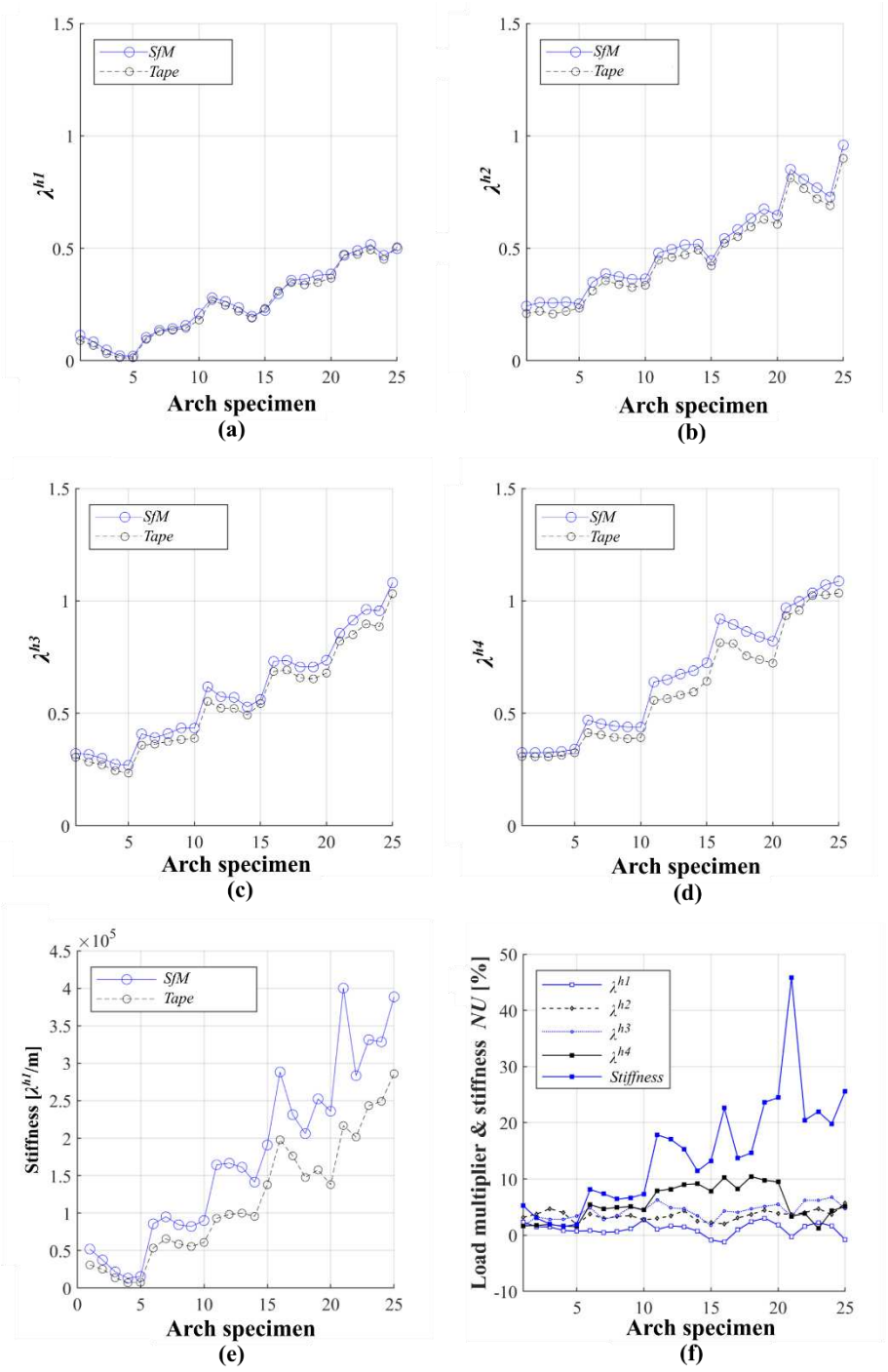

Figure 8. Influence of geometric uncertainty on: (a-d) load multipliers λ^{h1}, λ^{h2}, $\lambda^{h3}$and λ^{h4}; (e) stiffness of the arch; and (f) normalized uncertainty of load multipliers and stiffness.

7.3 Influence of geometrical uncertainty on the joint forces

Figure 9a-d shows the magnitude and distribution of the structural behaviour uncertainty for the joint forces at each hinge formation per arch specimen. From Figure 9a-d, the effect of geometric uncertainty: a) was significant on the joint forces and disproportionate to the geometric uncertainty, with a minima-maxima interval of normalized uncertainty calculated at -15% to 22% at each hinge formation; and b) remained quasi-constant and present for the all the loading phase. Thus, from the

above, geometrical uncertainty significantly influences the serviceability and ultimate limit state behaviour of arch specimens.

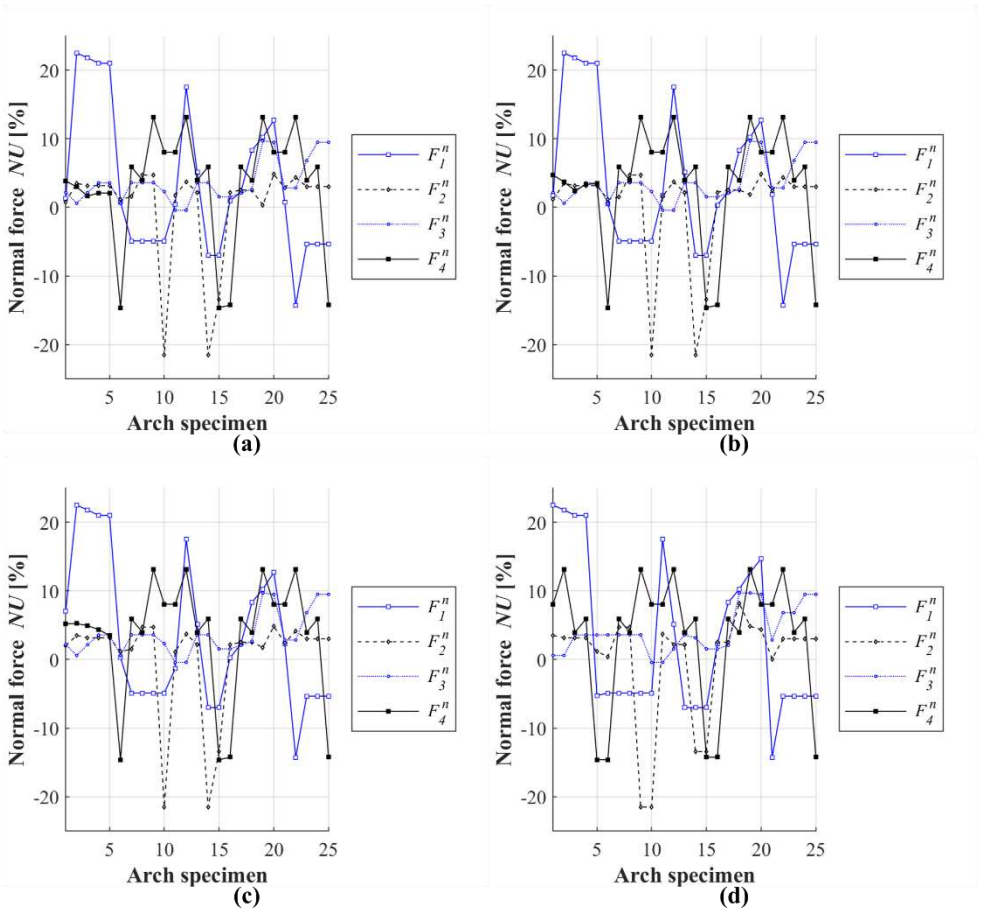

Figure 9. Influence of geometric uncertainty on joint forces: (a) first hinge formation ($\lambda = \lambda^{h1}$); (b) second hinge formation ($\lambda = \lambda^{h2}$); (c) third hinge formation ($\lambda = \lambda^{h3}$); and (d) fourth hinge formation ($\lambda = \lambda^{h4}$)

7.4 Correlation of geometric and structural behaviour uncertainty

A correlation coefficient equal to -0.84 was found for the normalized uncertainty of the joint inclination angle of the first joint, (i.e. joint dip J_1) and the normalized uncertainty of the 4th load multiplier λ^{h4} (i.e. collapse load). From Figure 10, a linear trend is visible between the two uncertainties. Namely, as the normalized uncertainty of joint dip J_1 decreases from zero, the normalized uncertainty of the 4th load multiplier λ^{h4} increases. Though other causes of structural behaviour uncertainty cannot be ruled out, this suggests that the most probable cause of load multiplier at the formation of the fourth hinge, uncertainty was the joint dip. This is in agreement with previous investigation [3-5] that stereotomy significantly influences the collapse load of arches. This finding suggests that, while developing the geometric model, particular care must be taken to obtain the accurate joint and block (especially joint inclination angle) to ascertain reliability on the predicted collapse load.

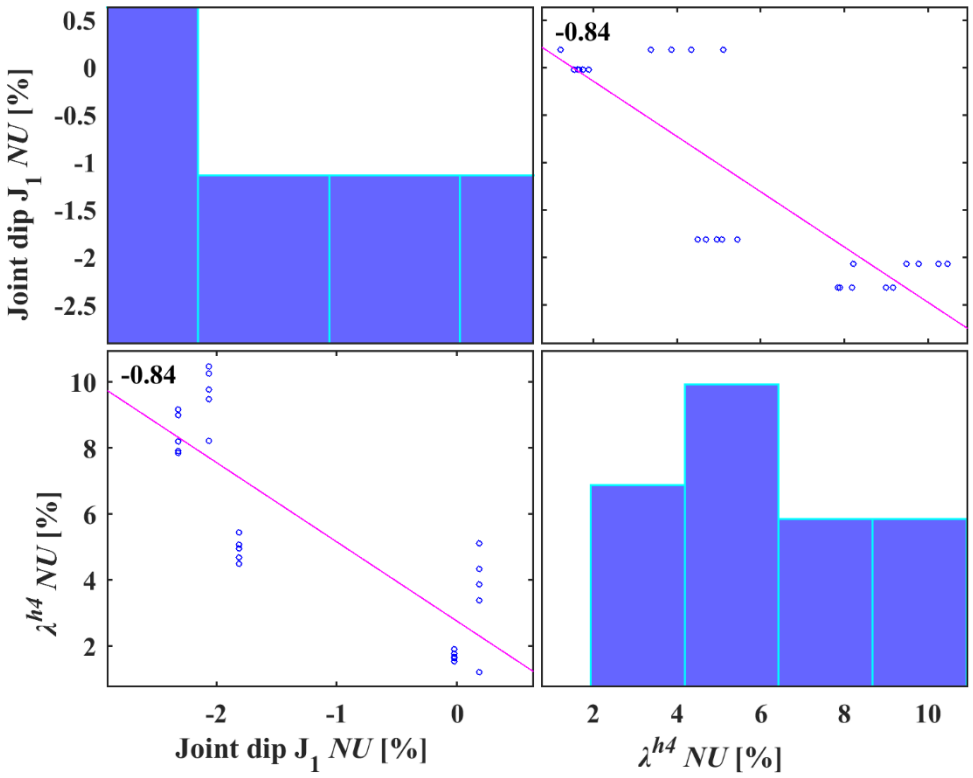

Figure 10. Correlation between geometric and structural behaviour uncertainty: Joint dip J_1 - load multiplier λ^{h4} (collapse load) correlation matrix.

8. Conclusions

This paper quantified the effect of geometric uncertainty on the structural behaviour of twenty-five arch specimens developed from SfM photogrammetry and tape measurements. The potential of the proposed "*Image2DEM*" framework was demonstrated for the geometrically accurate structural analysis with high-level numerical methods. In specific, a tilt-plane analysis numerically simulated with the DEM demonstrated that the stiffnesses (at the first hinge formation), loads multipliers, and normal forces (i.e. between joints) obtained with the proposed "*Image2DEM*" framework varied significantly, from those of traditional geospatial techniques (i.e. direct measurement with a tape).

Due to given differences between the geometric model derived from SfM photogrammetry and tape measurements (-4% to 9%), significant differences in: a) collapse load (-1% to 10%); b) stiffness (-2, 46%); and c) normal forces (-15, 22%) were found**.** Further than demonstrating the potential of the proposed **"***Image2DEM"* framework*,* these findings suggest that the employment of accurate geometric models (and subsequent geometric data acquisition techniques) is generally important to obtain accuracy in the structural behaviour of masonry and in-turn increase the reliability of the structural analysis. Furthermore, the geometrical uncertainty of the joints, and in specific, the joint inclination angle (i.e. joint dip) was found to directly influence the 4th load multiplier (i.e. collapse load), with a linear trend. Thus, while developing the geometric model, particular care must be taken to obtain the accurate geometrical properties of the joints as well.

Future research is planned to examine the validity of these finding on large-scale structures, yet this contribution paves the way for reliable and methodical structural analysis. Extrapolating the results to different geometries and different load configurations would require additional numerical and experimental investigations. While this work presented a deterministic quantification of the effect of

geometric uncertainty, a future investigation is recommended to either combine or compare its approach with that of a probabilistic framework, such as developed by Cavalagli *et al.* [8]. Thereafter, an inherent limitation of employing orthoimages for developing geometric models is also made apparent here. Specifically, the description of the structure limited to two-dimensions, since two-dimensional metric information is employed. Future research is recommended to overcome the aforementioned limitations through both geometrical modifications within the DEM software (i.e. splitting the geometric model along the transverse axis) and the employment of orthoimagery containing transverse axis data (i.e. such as digital elevation models). Additionally, future study should be carried out to explicitly examine the internal precision of the SfM photogrammetry pipeline on masonry structures, in a common spirit with the aforementioned geomorphological studies (i.e. [57]). Finally, a recommendation is also made to automate the proposed framework, by augmenting the process of block segmentation. Machine learning techniques, as in [71], have been identified as candidates for automated block segmentation.

9. Acknowledgements

The work presented in this paper has been financially supported by an EPRSC doctoral training award (case/179/65/82). The authors also gratefully acknowledge Gabriel Lee Stockdale and Prof Gabriele Milani for providing the experimental data and Mr James Goodyear for guiding the SfM photogrammetry carried out at Structures Laboratory, Newcastle University.

10. References

[1] P. Lourenco, Computations on historic masonry structures, Progress in Structural Engineering and Materials 4 (2002), pp. 301-319, DOI: 10.1002/pse.120

[2] J. Heyman, The safety of masonry arches, International Journal of Mechanical Sciences 11 (4) (1969), pp. 363-385, DOI: 10.1016/0020-7403(69)90070-8

[3] N. Makris, H. Alexakis, The effect of stereotomy on the shape of the thrust-line and the minimum thickness of semicircular masonry arches, Archive of Applied Mechanics 83 (10) (2013), pp. 1511-1533, DOI: 10.1007/s00419-013-0763-4

[4] D. Nikolić, Thrust line analysis and the minimum thickness of pointed masonry arches, Acta Mechanica 228 (6) (2017), pp. 2219-2236, DOI: 10.1007/s00707-017-1823-6

[5] O. Gáspár, A.A. Sipos, I. Sajtos, Effect of stereotomy on the lower bound value of minimum thickness of semi-circular masonry arches, International Journal of Architectural Heritage 12 (6) (2018), pp. 899-921, DOI: 10.1080/15583058.2017.1422572

[6] H. Alexakis, N. Makris, Limit equilibrium analysis and the minimum thickness of circular masonry arches to withstand lateral inertial loading, Archive of Applied Mechanics 84 (5) (2014), pp. 757-772, DOI: 10.1007/s00419-014-0831-4

[7] N. Cavalagli, V. Gusella, L. Severini, Lateral loads carrying capacity and minimum thickness of circular and pointed masonry arches, International Journal of Mechanical Sciences 115-116 (2016), pp. 645-656, DOI: 10.1016/j.ijmecsci.2016.07.015

[8] N. Cavalagli, V. Gusella, L. Severini, The safety of masonry arches with uncertain geometry, Computers & Structures 188 (2017), pp. 17-31, DOI: 10.1016/j.compstruc.2017.04.003

[9] A. Zanaz, S. Yotte, F. Fouchal, A. Chateauneuf, Efficient masonry vault inspection by Monte Carlo simulations: Case of hidden defect, Case Studies in Structural Engineering 5 (2016), pp. 1-12, DOI: 10.1016/j.csse.2015.12.001

[10] P. Zampieri, N. Simoncello, C. Pellegrino, Seismic capacity of masonry arches with irregular abutments and arch thickness, Construction and Building Materials 201 (2019), pp. 786-806, DOI: 10.1016/j.conbuildmat.2018.12.063

[11] P. Zampieri, N. Cavalagli, V. Gusella, C. Pellegrino, Collapse displacements of masonry arch with geometrical uncertainties on spreading supports, Computers & Structures 208 (2018), pp. 118-129, DOI: 10.1016/j.compstruc.2018.07.001
[12] L. Severini, N. Cavalagli, M. DeJong, V. Gusella, Dynamic response of masonry arch with geometrical irregularities subjected to a pulse-type ground motion, Nonlinear Dynamics 91 (2017), pp. 609–624, DOI: 10.1007/s11071-017-3897-z
[13] F. Szakály, Z. Hortobágyi, K. Bagi, Discrete element analysis of the shear resistance of planar walls with different bond patterns, The Open Construction and Building Technology Journal 10 (2016), pp. 220-232, DOI: 10.2174/1874836801610010220
[14] R. Napolitano, B. Glisic, Understanding the function of bonding courses in masonry construction: An investigation with mixed numerical methods, Journal of Cultural Heritage 39 (2019), pp. 120-129, DOI: 10.1016/j.culher.2019.03.007
[15] M. Godio, I. Stefanou, K. Sab, Effects of the dilatancy of joints and of the size of the building blocks on the mechanical behavior of masonry structures, Meccanica 53 (7) (2018), pp. 1629-1643, DOI: 10.1007/s11012-017-0688-z
[16] T. Forgács, V. Sarhosis, K. Bagi, Influence of construction method on the load bearing capacity of skew masonry arches, Engineering Structures 168 (2018), pp. 612-627, DOI: 10.1016/j.engstruct.2018.05.005
[17] B. Pulatsu, E. Erdogmus, P.B. Lourenco, Comparison of in-plane and out-of-plane failure modes of masonry arch bridges using discontinuum analysis, Engineering Structures 178 (2019), pp. 24-36, DOI: 10.1016/j.engstruct.2018.10.016
[18] M. Naderi, M. Zekavati, Assessment of seismic behavior stone bridge using a finite element method and discrete element method, Earthquakes and Structures 14 (4) (2018), pp. 297-303, DOI: 10.12989/eas.2018.14.4.297
[19] D. Foti, V. Vacca, I. Facchini, DEM modeling and experimental analysis of the static behavior of a dry-joints masonry cross vaults, Construction and Building Materials 170 (2018), pp. 111-120, DOI: 10.1016/j.conbuildmat.2018.02.202
[20] T.T. Bui, A. Limam, V. Sarhosis, M. Hjiaj, Discrete element modelling of the in-plane and out-of-plane behaviour of dry-joint masonry wall constructions, Engineering Structures 136 (2017), pp. 277-294, DOI: 10.1016/j.engstruct.2017.01.020
[21] R. Napolitano, B. Glisic, Methodology for diagnosing crack patterns in masonry structures using photogrammetry and distinct element modeling, Engineering Structures 181 (2019), pp. 519-528, DOI: 10.1016/j.engstruct.2018.12.036
[22] R. Napolitano, M. Hess, B. Glisic, Quantifying the differences in documentation and modeling levels for building pathology and diagnostics, Archives of Computational Methods in Engineering (2019), pp. 1-18, DOI: 10.1007/s11831-019-09350-y
[23] R.K. Napolitano, M. Hess, B. Glisic, The foundation walls of the baptistery Di San Giovanni: A combination of laser scanning and finite-distinct element modeling to ascertain damage origins, International Journal of Architectural Heritage 13 (7) (2019), pp. 1180-1193, DOI: 10.1080/15583058.2019.1582726
[24] M.J. Westoby, J. Brasington, N.F. Glasser, M.J. Hambrey, J.M. Reynolds, 'Structure-from-Motion' photogrammetry: A low-cost, effective tool for geoscience applications, Geomorphology 179 (2012), pp. 300-314, DOI: 10.1016/j.geomorph.2012.08.021
[25] J. Mills, D. Barber, Geomatics techniques for structural surveying, Journal of surveying engineering 57 (2004), pp. 56-64 DOI: 10.1061/(ASCE)0733-9453(2004)130:2(56)
[26] C. Altuntas, M.E. Pehlivanlı, S. Kurban, Low-cost 3D imaging and measurement techniques for documentation of Meram masonry arch bridge in Turkey, International Journal of Sensors and Sensor Networks Journal of Sensors and Sensor Networks 5 (2017), pp. 63-69, DOI: 10.11648/j.ijssn.20170505.11

[27] V. Barrile, G. Bilotta, A. Nunnari, UAV and computer vision, detection of infrastructure losses and 3D modeling, ISPRS Annals of Photogrammetry, Remote Sensing and Spatial Information Sciences, Vol. IV-4/W4, Safranbolu, Karabuk, Turkey, 2017, pp. 135-139
[28] V. Barrile, G. Candela, A. Fotia, Point cloud segmentation using image processing techniques for structural analysis, ISPRS - International Archives of the Photogrammetry, Remote Sensing and Spatial Information Sciences, Vol. XLII-2/W11, Milan, Italy, 2019, pp. 187-193
[29] S. Chen, D. Laefer, E. Mangina, I. Zolanvari, J. Byrne, UAV bridge inspection through evaluated 3D reconstructions, Journal of Bridge Engineering 24 (2019), p. 05019001, DOI: 10.1061/(ASCE)BE.1943-5592.0001343
[30] T. Hinks, Geometric processing techniques for urban aerial laser scan data, Ph.D., College of Engineering, Mathematical and Physical Sciences School of Computer Science and Informatics, University College Dublin, 2011. URL: https://tommyhinks.files.wordpress.com/2012/02/thinks-thesis-single.pdf [Accessed 5th December 2019]
[31] G. Castellazzi, M.A. Altri, G. Bitelli, I. Selvaggi, A. Lambertini, From laser scanning to finite element analysis of complex buildings by using a semi-automatic procedure, Sensors 15 (8) (2015), pp. 18360–18380, DOI: 10.3390/s150818360
[32] G. Bitelli, G. Castellazzi, A. D'Altri, S. Miranda, A. Lambertini, I. Selvaggi, Automated voxel model from point clouds for structural analysis of cultural heritage, ISPRS XL1 - International Archives of the Photogrammetry, Remote Sensing and Spatial Information Sciences, Vol. XLI-B5, Prague, Czech republic, 2016, pp. 191-197
[33] G. Castellazzi, A.M. D'Altri, S. de Miranda, F. Ubertini, An innovative numerical modeling strategy for the structural analysis of historical monumental buildings, Engineering Structures 132 (2017), pp. 229-248, DOI: 10.1016/j.engstruct.2016.11.032
[34] B. Conde, L. F. Ramos, D. Oliveira, B. Riveiro, M. Solla, Structural assessment of masonry arch bridges by combination of non-destructive testing techniques and three-dimensional numerical modelling: Application to Vilanova bridge, Engineering Structures 148 (2017), pp. 621-638, DOI: 10.1016/j.engstruct.2017.07.011
[35] A.M. D'Altri, G. Milani, S. Miranda, G. Castellazzi, V. Sarhosis, Stability analysis of leaning historic masonry structures, Automation in Construction 92 (2018), pp. 199–213, DOI: 10.1016/j.autcon.2018.04.003
[36] L.J. Sánchez-Aparicio, B. Riveiro, D. González-Aguilera, L.F. Ramos, The combination of geomatic approaches and operational modal analysis to improve calibration of finite element models: A case of study in Saint Torcato Church (Guimarães, Portugal), Construction and Building Materials 70 (2014), pp. 118-129, DOI: 10.1016/j.conbuildmat.2014.07.106
[37] L. Sánchez-Aparicio, A. Villarino, J.M. García Gago, D. González-Aguilera, Photogrammetric, geometrical, and numerical strategies to evaluate initial and current conditions in historical constructions: A test case in the church of san lorenzo (Zamora, Spain), Remote Sensing 8(1) (2016), p. 60, DOI: 10.3390/rs8010060
[38] M. Korumaz, M. Betti, A. Conti, G. Tucci, G. Bartoli, V. Bonora, A.G. Korumaz, L. Fiorini, An integrated Terrestrial Laser Scanner (TLS), Deviation Analysis (DA) and Finite Element (FE) approach for health assessment of historical structures. A minaret case study, Engineering Structures 153 (2017), pp. 224-238, DOI: 10.1016/j.engstruct.2017.10.026
[39] R. Rolin, E. Antaluca, J.L. Batoz, F. Lamarque, M. Lejeune, From point cloud data to structural analysis through a geometrical hbim-oriented model, Journal of Computational Cultural Heritage 12 (2) (2019), pp. 1-26, DOI: 10.1145/3242901
[40] V. Acary, J. Blaise, P. Drap, M. Florenzano, S. Garrec, M. Jean, NSCD method applied to mechanical simulation of masonry in historical buildings using MOMA, International Symposium WG3 on Simple methods for architectural photogrammetry, Olinda, Brazil, 1999, pp. 225-237

[41] B. Riveiro, J.C. Caamaño, P. Arias, E. Sanz, Photogrammetric 3D modelling and mechanical analysis of masonry arches: An approach based on a discontinuous model of voussoirs, Automation in Construction 20 (4) (2011), pp. 380-388, DOI: 10.1016/j.autcon.2010.11.008
[42] R. Napolitano, M. Hess, R. Coe-Scharff, B. Glisic, Numerical modeling of crack propagation in masonry structures, in: R. Aguilar, D. Torrealva, S. Moreira, M.A. Pando, L.F. Ramos (Eds.), Structural Analysis of Historical Constructions, Springer International Publishing, Cham, Switzerland, 2019, pp. 826-834.
[43] P. Morer, I. de Arteaga, J. Armesto, P. Arias, Comparative structural analyses of masonry bridges: An application to the Cernadela Bridge, Journal of Cultural Heritage 12 (3) (2011), pp. 300-309, DOI: 10.1016/j.culher.2011.01.006
[44] P. Morer, I. de Arteaga, A. Ortueta, A low-cost photogrammetric methodology to obtain geometrical data of masonry arch bridges, Journal of Architectural Conservation 19 (3) (2013), pp. 246-264, DOI: 10.1080/13556207.2013.869974
[45] M. Solla, J.C. Caamaño, B. Riveiro, P. Arias, A novel methodology for the structural assessment of stone arches based on geometric data by integration of photogrammetry and ground-penetrating radar, Engineering Structures 35 (2012), pp. 296-306, DOI: 10.1016/j.engstruct.2011.11.004
[46] B. Riveiro, M. Solla, I. de Arteaga, P. Arias, P. Morer, A novel approach to evaluate masonry arch stability on the basis of limit analysis theory and non-destructive geometric characterization, Automation in Construction 31 (2013), pp. 140-148, DOI: 10.1016/j.autcon.2012.11.035
[47] I. de Arteaga, P. Morer, The effect of geometry on the structural capacity of masonry arch bridges, Construction and Building Materials 34 (2012), pp. 97-106, DOI: 10.1016/j.conbuildmat.2012.02.037
[48] G. Stockdale, V. Sarhosis, G. Milani, Increase in seismic resistance for a dry joint masonry arch subjected to hinge control, 10th International Masonry Conference, Milan, Italy, 2018, pp. 968-981
[49] G. Misseri, M.J. DeJong, L. Rovero, Experimental and numerical investigation of the collapse of pointed masonry arches under quasi-static horizontal loading, Engineering Structures 173 (2018), pp. 180-190, DOI: 10.1016/j.engstruct.2018.06.009
[50] G. Tempesta, S. Galassi, Safety evaluation of masonry arches. A numerical procedure based on the thrust line closest to the geometrical axis, International Journal of Mechanical Sciences 155 (2019), pp. 206-221, DOI: 10.1016/j.ijmecsci.2019.02.036
[51] N.A. Nodargi, P. Bisegna, A unifying computational approach for the lower-bound limit analysis of systems of masonry arches and buttresses, Engineering Structures 221 (2020), p. 110999, DOI: 10.1016/j.engstruct.2020.110999
[52] S. Galassi, N. Ruggieri, G. Tempesta, A novel numerical tool for seismic vulnerability analysis of ruins in archaeological sites, International Journal of Architectural Heritage 14 (1) (2020), pp. 1-22, DOI: 10.1080/15583058.2018.1492647
[53] Y. Zhang, L. Macorini, B. Izzuddin, Mesoscale partitioned analysis of brick-masonry arches, Engineering Structures 124 (2016), pp. 142–166, DOI: 10.1016/j.engstruct.2016.05.046
[54] T. Forgacs, V. Sarhosis, K. Bagi, Minimum thickness of semi-circular skewed masonry arches, Engineering Structures 140 (2017), pp. 317-336, DOI: 10.1016/j.engstruct.2017.02.036
[55] Metashape Professional version 1.5.1 2019. URL: https://www.agisoft.com/buy/online-store/ [Accessed 19th January 2020]
[56] M. Pepe, I. Fregonese, N. Crocetto, Application of the SfM approach in building 3D models of masonry bridges using nadir, oblique and zenith images obtained from UAV aerial platform, IJCIET Volume 10, (3) (2019), pp. 1626 - 1638. URL: http://d.researchbib.com/f/9nq3q3YzyuMJ1yYzAioF9ALKA0MKWOMT1cov9IpTkiLJETo2kxMKViFHcQFHIHKmRjKmNmKmR2ZF9WFxAWEIEsZGOsZQAsZGLkYaOxMt.pdf [Accessed 23th April 2020]

[57] M.R. James, S. Robson, S. d'Oleire-Oltmanns, U. Niethammer, Optimising UAV topographic surveys processed with structure-from-motion: Ground control quality, quantity and bundle adjustment, Geomorphology 280 (2017), pp. 51-66, DOI: https://doi.org/10.1016/j.geomorph.2016.11.021

[58] A. Eltner, D. Schneider, Analysis of Different Methods for 3D Reconstruction of Natural Surfaces from Parallel-Axes UAV Images, The Photogrammetric Record 30 (151) (2015), pp. 279-299, DOI: 10.1111/phor.12115

[59] M.R. James, S. Robson, Straightforward reconstruction of 3D surfaces and topography with a camera: Accuracy and geoscience application, Journal of Geophysical Research: Earth Surface 117 (3) (2012), pp. 1-17, DOI: 10.1029/2011JF002289

[60] A. Eltner, A. Kaiser, C. Castillo, G. Rock, F. Neugirg, A. Abellán, Image-based surface reconstruction in geomorphometry - merits, limits and developments, Earth Surface Dynamics (2016), pp. 359–389, DOI: 10.5194/ESURF-4-359-2016

[61] M.R. James, S. Robson, M.W. Smith, 3-D uncertainty-based topographic change detection with structure-from-motion photogrammetry: precision maps for ground control and directly georeferenced surveys, Earth Surface Processes and Landforms 42 (12) (2017), pp. 1769-1788, DOI: 10.1002/esp.4125

[62] M.R. James, J.H. Chandler, A. Eltner, C. Fraser, P.E. Miller, J.P. Mills, T. Noble, S. Robson, S.N. Lane, Guidelines on the use of structure-from-motion photogrammetry in geomorphic research, Earth Surface Processes and Landforms 44 (10) (2019), pp. 2081-2084, DOI: 10.1002/esp.4637

[63] E. Sanz-Ablanedo, J. Chandler, J.R. Rodríguez-Pérez, C.J.R.S. Galán, Accuracy of Unmanned Aerial Vehicle (UAV) and SfM Photogrammetry Survey as a Function of the Number and Location of Ground Control Points Used, Remote Sensing 10 (2018), p. 1606, DOI: doi.org/10.3390/rs10101606

[64] F. Chiabrando, M. Turco, F. Rinaudo, Modeling the decay in an HBIM starting from 3D point clouds. A followed approach for cultural heritage knowledge, ISPRS - International Archives of the Photogrammetry, Remote Sensing and Spatial Information Sciences, Vol. XLII-2/W5, Ottawa, Canada, 2017, pp. 605-612

[65] E. Tsilimantou, E. Delegou, C. Ioannidis, A. Moropoulou, Geoinformation techniques for the 3D visualisation of historic buildings and representation of a building's pathology, 4th International Conference on Remote Sensing and Geoinformation of The Environment, Vol. 9688, SPIE, Paphos, Cyprus, 2016, pp. 1-9

[66] Autocad 2019, 2019. URL: https://www.autodesk.com/ [Accessed 13th July 2019]

[67] ITASCA. 3DEC 5.2 – Universal distinct element code manual. Theory and background. Mineapolis., 2019. URL: www.itasca.com [Accessed 19th January 2020]

[68] Matlab 2019 R2019b, 2019. URL: http://mathworks.com/ [Accessed]

[69] J.V. Lemos, Discrete element modeling of masonry structures, International Journal of Architectural Heritage 1 (2) (2007), pp. 190-213, DOI: 10.1080/15583050601176868

[70] M. Dejong, Seismic assessment strategies for masonry structures, Ph.D., Department of Architecture, Massachusetts Institute of Technology, 2009. URL: https://dspace.mit.edu/handle/1721.1/49538 [Accessed 19th January 2020]

[71] A. Forster, E. Valero, F. Bosché, Automated defect detection and classification in ashlar masonry walls using machine learning, Automation in Construction 106 (2019), p. 102846, DOI: 10.1016/j.autcon.2019.102846